

Calculation and prediction of divertor detachment via impurity seeding by using one-dimensional model

Wen-Jie Zhou(周文杰), Xiao-Ju Liu(刘晓菊), Xiao-He Wu(邬潇河), Bang Li(李邦), Qi-Qi Shi(石奇奇), Hao-Chen Fan(樊皓尘), Yan-Jie Yang(杨艳杰), and Guo-Qiang Li(李国强)
Citation: Chin. Phys. B, 2024, 33 (**8**): 085205. DOI: 10.1088/1674-1056/ad426a

What follows is a list of articles you may be interested in

Evolution of the high-field-side radiation belts during the neon seeding plasma discharge in EAST tokamak

Ji-Chan Xu(许吉禅), Liang Wang(王亮), Guo-Sheng Xu(徐国盛), Yan-Min Duan(段艳敏), Ling-Yi Meng(孟令义), Ke-Dong Li(李克栋), Fang Ding(丁芳), Rui-Rong Liang(梁瑞荣), Jian-Bin Liu(刘建斌), and EAST Team
Chin. Phys. B, 2022, 31 (**10**): 105203. DOI: 10.1088/1674-1056/ac935a

Study on divertor plasma behavior through sweeping strike point in new lower divertor on EAST

Yu-Qiang Tao(陶余强), Guo-Sheng Xu(徐国盛), Ling-Yi Meng(孟令义), Rui-Rong Liang(梁瑞荣), Lin Yu(余林), Xiang Liu(刘祥), Ning Yan(颜宁), Qing-Quan Yang(杨清泉), Xin Lin(林新), and Liang Wang(王亮)
Chin. Phys. B, 2022, 31 (**6**): 065204. DOI: 10.1088/1674-1056/ac4a65

Hardening effect of multi-energy $^{W2+}$-ion irradiation on tungsten–potassium alloy

Yang-Yi-Peng Song(宋阳一鹏), Wen-Bin Qiu(邱文彬), Long-Qing Chen(陈龙庆), Xiao-Liang Yang(杨晓亮), Hao Deng(邓浩), Chang-Song Liu(刘长松), Kun Zhang(张坤)†, and Jun Tang(唐军)‡
Chin. Phys. B, 2020, 29 (**10**): 105202. DOI: 10.1088/1674-1056/ab9c09

Observation of deuterium molecule emission spectra under an active feedback control of H-mod plasma divertor detachment experiment on the EAST tokamak

Wei Gao(高伟), Juan Huang(黄娟), Jichan Xu(许吉禅), Liang Wang(王亮), Jing Zhang(张静), Jianxun Su(宿建勋), Yingjie Chen(陈颖杰), Wei Gao(高伟), Zhenwei Wu(吴振伟), EAST Team
Chin. Phys. B, 2019, 28 (**12**): 125202. DOI: 10.1088/1674-1056/ab54b2

Numerical study of influence of *J*×*B* force on melt layer under conditions relevant to ITER ELMs

Yan Huang(黄艳), Ji-Zhong Sun(孙继忠), Juan Cai(蔡娟), Zhen-Yue Sun(孙振月), Chao-Feng Sang(桑超峰), De-Zhen Wang(王德真)
Chin. Phys. B, 2019, 28 (**4**): 045201. DOI: 10.1088/1674-1056/28/4/045201

Calculation and prediction of divertor detachment via impurity seeding by using one-dimensional model

Wen-Jie Zhou(周文杰)[1,2], Xiao-Ju Liu(刘晓菊)[1,†], Xiao-He Wu(邬潇河)[1,2], Bang Li(李邦)[1,2], Qi-Qi Shi(石奇奇)[1,2], Hao-Chen Fan(樊皓尘)[1,2], Yan-Jie Yang(杨艳杰)[1,2], and Guo-Qiang Li(李国强)[1,‡]

[1] *Institute of Plasma Physics, Hefei Institutes of Physical Science, Chinese Academy of Sciences, Hefei* 230031, *China*
[2] *University of Science and Technology of China, Hefei* 230026, *China*

(Received 25 January 2024; revised manuscript received 16 April 2024; accepted manuscript online 24 April 2024)

Achieving the detachment of divertor can help to alleviate excessive heat load and sputtering problems on the target plates, thereby extending the lifetime of divertor components for fusion devices. In order to provide a fast but relatively reliable prediction of plasma parameters along the flux tube for future device design, a one-dimensional (1D) modeling code for the operating point of impurity seeded detached divertor is developed based on Python language, which is a fluid model based on previous work (*Plasma Phys. Control. Fusion* **58** 045013 (2016)). The experimental observation of the onset of divertor detachment by neon (Ne) and argon (Ar) seeding in EAST is well reproduced by using the 1D modeling code. The comparison between the 1D modeling and two-dimensional (2D) simulation by the SOLPS-ITER code for CFETR detachment operation with Ne and Ar seeding also shows that they are in good agreement. We also predict the radiative power loss and corresponding impurity concentration requirement for achieving divertor detachment via different impurity seeding under high heating power conditions in EAST and CFETR phase II by using the 1D model. Based on the predictions, the optimized parameter space for divertor detachment operation on EAST and CFETR is also determined. Such a simple but reliable 1D model can provide a reasonable parameter input for a detailed and accurate analysis by 2D or three-dimensional (3D) modeling tools through rapid parameter scanning.

Keywords: divertor detachment, impurity seeding, one-dimensional modeling

PACS: 52.55.Rk, 52.65.–y, 52.55.Fa **DOI:** 10.1088/1674-1056/ad426a

1. Introduction

The divertor is an important component of modern magnetic confinement fusion devices. For ITER[1] and China future fusion device CFETR[2] with high heating power and density discharges, the excessive heat load on the divertor target and the erosion problems of the target materials are the main challenges affecting the high performance and long pulse operation. In addition, to mitigate or eliminate the erosion of target plate materials, the divertor needs operating at least in the partial detachment to maintain a low plasma temperature at the divertor plates. It is essential to inject impurity gas with high radiative loss rate and low co-deposition with tritium to increase the power dissipation in tokamak, especially in the divertor region, and eventually reducing the peak heat load deposited on the divertor target. The optimal candidates for radiation cooling are noble gas, such as neon (Ne), argon (Ar), and krypton (Kr). The effect of impurity seeding on divertor detachment has been investigated on many tokamaks, such as AUG,[3] DIII-D,[4] JET,[5] JT-60U,[6] EAST,[7] and C-Mod,[8] via experiment and simulation. The steady and influential progress has been made in 2D modelling of divertor research,[9–11] but 2D model calculations require a lot of computational sources, which is not conducive to quick parameter scanning and parameter prediction. And some 1D analytic and computational models of the divertor plasma have been developed previously.[12–17] These 1D codes provide an insight into the research on divertor plasma dynamics, such as the role of different atomic and molecular processes in detachment and the effects of the neutrals on detachment fronts. In addition, there are a number of zero-dimensional (0D) stationary models[18–20] containing impurity radiation, which involve the investigation of the power exhausted on the divertor plates, such as the evaluation of the detachment degree, which may have a positive effect on the preliminary design work of fusion reactors. It has been shown that impurity seeding in the fusion reactor has a significant effect on the high heat flux mitigation and the achievement of divertor detachment.[19] Therefore, impurity seeding is inevitable for divertor detachment with the high parameter discharges, especially for ITER, EU-DEMO,[21] and CFETR. Here, in order to provide a simple but relatively reliable prediction of plasma parameters for the impurity seeded detached divertor operational point for fusion devices, a 1D modeling code is developed based on the Python language.

In the 1D model, the divertor plasma is approximately represented by a flux tube with the width $\lambda_{\rm int}$[22] in the outer scrape-off layer (SOL). The momentum losses, ionization source, and heat flux dissipation are adequately considered in

†Corresponding author. E-mail: julie1982@ipp.ac.cn
‡Corresponding author. E-mail: ligq@ipp.ac.cn

© 2024 Chinese Physical Society and IOP Publishing Ltd

our model. This 1D model can calculate and predict the evolution of plasma parameters along the flux tube from divertor target to the outer mid-plane (OMP) under different divertor detachment operational points.

The rest of the paper is organized as follows. Section 2 primarily provides an overview of the physics model for the 1D modeling. The comparison between the 1D model and the EAST experiments is presented in Subsection 3.1. And the calculation of divertor detachment for CFETR by the 1D model and 2D transport code are compared in Subsection 3.2. Section 4 shows the prediction and parameter scanning with the 1D modeling for the high heating power scenarios on EAST and CFETR phase II with high fusion power scenarios, respectively. Finally, the conclusion is given in Section 5.

2. Physics model for 1D SOL modeling

The 1D model mainly focus on the region of the first e-folding length of the heat flux of outside the separatrix.[23,24] A flux tube with length L establishes a connection between the OMP and the divertor target. The flux tube geometry of EAST applied to the 1D modeling is depicted in Fig. 1. The cross-section of the tube is determined by the following factors: the toroidal circumference, which is proportional to the large radius R, the mid-plane heat flux width λ_q[22] and the pitch factor $\sin(\tan^{-1}(B_p/B_t)$ of the magnetic field lines. At the divertor inlet, the parallel heat flux is assumed to broaden instantaneously with width from λ_q to λ_{int} as shown by the red arrows in Fig. 1. At the target, power width λ_{int} is broadened due to the effect of the power spreading S, and can be obtained from $\lambda_{int} = \lambda_q + 1.64S$.[25] The parallel heat flux width λ_q can be obtained through divertor probe diagnostics or infrared camera measurements. The experimental results of existing tokamak devices are in good agreement with the Eich's experimental scaling that λ_q decreases linearly as the poloidal magnetic field B_{pol} (or equivalently the plasma current) increases.[26] The simulation results based on BOUT++ show that for future devices such as CFETR, the boundary cross-field transport may change from a drift-dominated regime into a turbulence-dominated regime.[27] In this case, the value of λ_q will be much larger than the extrapolated value from the Eich's experimental scaling. The divertor region is generally considered to be the area at a distance of $x \le L_{div}$ from the strike point, where L_{div} is defined as the distance from the target to the divertor entrance. The value of L_{div} varies with tokamak size. Radiation generated in $x \le L_{div}$ is regarded as divertor radiation.

The evolutions of the neutral particle and the ion flux along the flux tube, considering the ionization and recombination processes, are given by

$$\frac{\partial}{\partial x} n_0 = -\frac{R_{ion} n_e n_0}{v_0} + \frac{R_{rec} n_e n_i}{v_0}, \tag{1}$$

$$\frac{\partial}{\partial x}(nv) = R_{ion} n_e n_0 - R_{rec} n_e n_i. \tag{2}$$

Here, v_0 represents the neutral particle velocity in Eq. (1), which is assumed to be $1/4$ of the average thermal speed along the flux tube, i.e., $v_0 = (1/4)\sqrt{8eT_0/(\pi m_0)}$, representing the reflection of sheath accelerated ions and Franck–Condon neutrals.[25] Integrating continuity equation (2), the ion flux towards the target can be obtained. This equation can also be used to calculate the plasma flow velocity v.

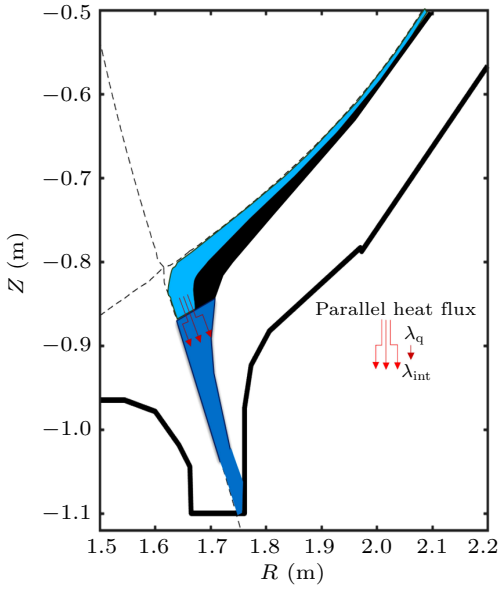


Fig. 1. Geometry of flux tube of EAST applied to 1D modeling. At the divertor inlet, the parallel heat flux is assumed to broaden instantaneously. The red arrow indicates the heat flow width broadening from λ_q to λ_{int}. In the flux tube of the EAST with $q_{95} = 4.5$, the connection length from the target to the OMP is approximately 25 m. The connection length is the calculation length for the 1D model.

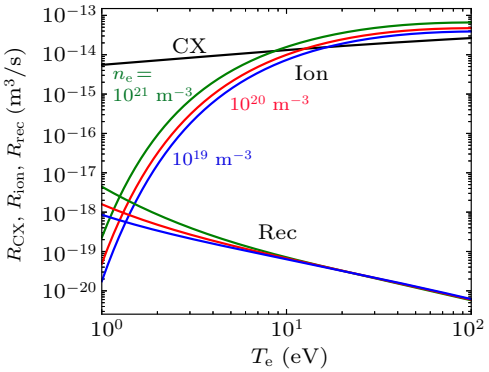


Fig. 2. Hydrogen atom effective ionization, charge exchange (CX), and recombination (Rec) rate coefficients taken from ADAS, as a function of electron temperature for electron density $n_e = 10^{21}$ m^{-3}, $n_e = 10^{20}$ m^{-3}, and $n_e = 10^{19}$ m^{-3}.

The dissipation of heat flux is mainly caused by impurity radiation, charge exchange, and ionization loss,

$$\frac{\partial q_{\parallel}}{\partial x} = n_e^2 c_Z L_Z(T_e) + eT_i R_{CX} n_i n_0 + eE_{ion} R_{ion} n_e n_0 - \frac{\partial q_{conv}}{\partial x}, \tag{3}$$

where q_{conv} represents the convective heat flux, specifically, $q_{conv} = (5eTn + \frac{1}{2} m_i n v^2)v$, which has to be fed by the upstream $q_{||}$. At low T_e, heat is transported mainly by convec-

tion, $R_{\rm ion}$ is the reaction rate of ionization, $R_{\rm rec}$ is recombination rate, $R_{\rm CX}$ is the charge exchange rate, L_Z is the impurity radiative cooling rate, and $\bar{Z}$ is their mean charge number used in the equations, whose values are cited from ADAS databases.[28] Figure 2 shows the temperature-dependent ionization, recombination and the effective charge exchange rates of hydrogen under different densities. Variations in electron density are not considered separately when evaluating the radiative cooling rate of impurities L_Z, instead a fixed electron density of 10^{20} m^{-3} is used, which is a typical value in the SOL region.[29] The enhancement in radiation power caused by non-coronal effect is represented approximately by setting non-coronal parameters $n_{\rm e}\cdot\tau = 10^{20}$ m$^{-3}\times 0.5$ ms.[30] Figure 3(a) shows the temperature-dependent impurity radiation loss for different non-coronal parameters. As shown in the figure, the non-coronal effects are relatively weak at temperatures below 10 eV and become more pronounced above 10 eV. The accurate specification of residence time τ is challenging, considering the detached scenario in our study, the electron temperature near the target is lower, leading to relatively mild non-coronal effects. In order to more accurately handle the effective τ, it is necessary to perform time-dependent and position-dependent calculations of the impurity state population equation and plasma background.[25] In this paper, $n_{\rm i} = n_{\rm e}$, $n_z = c_Z n_{\rm e}$. Here, c_Z is expressed as the impurity concentration without consideration of the dilution by impurities. To distinguish between species engaged in certain physical processes, the indices i and e are marked.

According to the thermal conduction equation, we can obtain the temperature drop along the flux tube from upstream, as expressed in Eq. (4). In the 1D model, the ion temperature is assumed to be equal to the electron temperature, that is, $T = T_{\rm i} = T_{\rm e}$, satisfying the following equation:

$$\frac{\partial}{\partial x}T_{\rm e}^{7/2} = -\frac{7}{2}\frac{q_{||}}{\kappa_0} \approx -\frac{7}{2}\cdot\frac{q_{\parallel}}{2390\cdot Z_{\rm eff}^{-0.3}}, \tag{4}$$

where $Z_{\rm eff}^{-0.3}$ approximates the thermal conductivity decreasing with $Z_{\rm eff} = \sum_i n_{\rm i}\bar{Z}_{\rm i}^{\,2}/n_{\rm e}$ increasing.[30] The mean charge number $\bar{Z}$ of impurity is related to the electron temperature and value of $n_{\rm e}\tau$ as shown in Fig. 3(b). In the 1D modeling, the upstream parallel heat flux starting from the target plate is obtained and related to the total power crossing the separatrix $P_{\rm sep}$.

Assuming that the Mach number $M = 1$ at the target, which is given by the formula $M = v/c_{\rm s}$, where $c_{\rm s}$ is the thermal sound speed and expressed as $c_{\rm s} = \sqrt{2eT}/m_{\rm i}$. The momentum conservation relationship is written as

$$\frac{\partial}{\partial x}(n(m_{\rm i}v^2 + 2eT)) = -m_{\rm i}vR_{\rm CX}n_{\rm i}n_0 - m_{\rm i}vR_{\rm rec}n_{\rm e}n_{\rm i}. \tag{5}$$

According to the two-point model (TPM), if there is no loss of momentum, the upstream and target static pressure satisfy the relationship $2T_{\rm tar}n_{\rm tar} = T_{\rm up}n_{\rm up}$.[31] The plasma flow toward the target plate may lose momentum due to frictional collisions with neutrals and recombination,[32] especially for the detached plasma regime. In the 1D model, the momentum loss terms mainly include charge exchange and recombination.

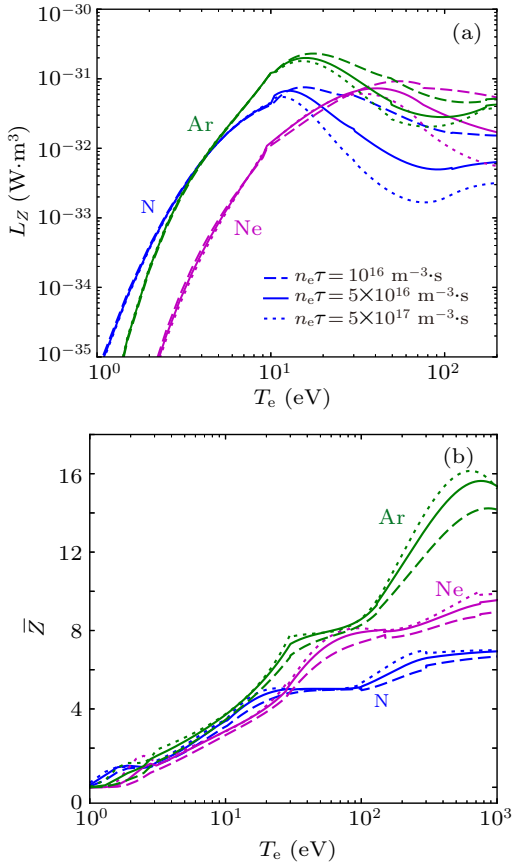


Fig. 3. (a) Radiative cooling rates and (b) mean charge numbers *versus* electron temperature for various values of non-coronal parameter $n_{\rm e}\tau$, with solid line representing the result for the non-coronal parameter $n_{\rm e}\tau = 0.5$ ms $\times\, 10^{20}$ m^{-3}, which is used in this research, and dotted and dashed lines for each species corresponding to $n_{\rm e}\tau = 0.5$ ms $\times\, 10^{21}$ m^{-3} and $n_{\rm e}\tau = 0.1$ ms $\times\, 10^{20}$ m^{-3}, respectively.

The power $P_{\rm up}$ transported from the core plasma is delivered to the end of the flux tube located at the OMP and expressed as[25]

$$q_{\parallel} = P_{\rm up}/\left(2\pi R_{\rm omp}\lambda_{\rm q}\sin\left(\tan^{-1}\left(B_{\rm p}/B_{\rm t}\right)\right)\right). \tag{6}$$

Due to the fact that the 1D model can only calculate parallel heat flux with the width $\lambda_{\rm q}$, the calculated upstream power $P_{\rm up}$ only represents a fraction $1-1/{\rm e}$ of the power reaching to the outer divertor. Assuming that the ratio of the power flowing to the inner divertor to that to outer divertor is 1:2,[25] the total power at the target plate is 1.5 times the power to the outer divertor. This is normally reasonable for the discharge with a favorable toroidal magnetic field ($B_{\rm t}$) configuration (i.e., ion $B\times\nabla B$ drift pointing towards the X-point). In this case, particles flow from the outer divertor to the inner divertor driven by $E\times B$ drifts, resulting in a relative large heat flux deposited at the outer divertor target.[33] Many tokamaks have experimentally observed that the L–H threshold power

$(P_{L\to H})$ is lower for the favorable B_t configuration than for the unfavorable B_t configuration.[34] In addition, discharges under favorable B_t configuration are also beneficial to high plasma performance.[35] Therefore, a majority of current tokamak devices operate under favorable B_t configuration, the CFETR is also designed to operate with favorable B_t configuration.[2] Therefore, the value of P_{sep} can be approximately calculated from the formula $P_{sep} = f_{out}P_{up}$, where the power fraction f_{out} is $1.5/(1-1/e)$. The cross-sectional area of the flux tube A_{cross} is represented by the denominator part of Eq. (6). The total parallel heat flux density $q_{||total}$ reaching the target can be measured by the Langmuir probes on the target plates.[7] The perpendicular heat flux density reaching the target is given by $q_{\perp,tar} = q_{||total}\sin\alpha$, where $q_{||total} = q_{||} + q_{conv}$, and $\alpha \approx 3^\circ$ that is the grazing angle between the target and the magnetic field line, a typical value for EAST discharges with the strike point on the vertical target plate.[36]

The temperature, heat flux, and particle flux on the divertor target plates are selected as the boundary conditions for solving the 1D equations. On the one hand, compared with the temperature and density that are uncertain in the experimental measurement at the upstream plasma, the parameters on the target are easily obtained through the boundary diagnostic system such as the divertor probe diagnostics or infrared camera measurements. On the other hand, setting reasonable plasma parameters at the target is conducive to the simulation research of various scenarios of detachment. Since the target plate is chosen as the starting point for the calculation of the 1D model, the plasma flow velocity v in Eq. (2) is negative because it always points to the target plate in 1D model, and the loss terms associated with momentum and power are naturally regarded as source terms in the above equation. When using 1D model, it should be noted that it does not include perpendicular plasma or neutral transport. Furthermore, the broadening of power width is only a simple treatment, it is not fully understood so far.

Table 1. Input and output physical parameters of 1D modeling code.

	Physical parameter	Description
Input	$T_{e,tar}$	electron temperature at target
	$q_{\perp,tar}$	perpendicular heat flux density at target
	Γ_0 or Γ_{ion}	ion flux/neutral flux
	λ_q, λ_{int}	power widths
	C_z	impurity concentrations
	L_{div}	divertor region parallel length
	$L_{||}$	connection length from SOL to divertor target
Output	P_{up} or P_{sep}	upstream power/total separatrix power
	T_e	upstream electron temperature
	q_{rad}	impurity radiation power density
	n_e	upstream density

The input and output physical parameters of the 1D modeling code are listed in Table 1. The ion flux and neutral flux are assumed to be equal. Depending on the boundary condition of the sheath $q_{||} = \gamma_s\Gamma_{ion}kT_{e,tar}$, any one of temperature, heat flux, and ion flux can be obtained by combining the other two. In this paper, the temperature unit and energy unit are both in unit eV, while other units are in the SI units.

3. Validation of 1D model

3.1. Comparison of 1D model and EAST experiments

In order to accurately reproduce EAST divertor detachment by using the 1D model, it is essential to set the input parameters of the model in accordance with the experimentally measured values. The input temperature and heat flux density of the 1D model are taken from the measurements of the divertor Langmuir probes in EAST. The reliability of the 1D model can be verified by comparing the upstream power and temperature calculated by the model with the experimental values.

Shot #57417 is a typical upper single null configuration H-mode discharge with Ar impurity seeding in EAST.[37] The basic parameters for this shot are as follows: the energy confinement factor $H_{98,y2} \sim 0.8$, the plasma current $I_p = 400$ kA, the toroidal magnetic field $B_t = 2.3$ T, and the line average electron density $\bar{n}_e = 4.5\times10^{19}$ m^{-3}. The injected power $P_{in} = 4.3$ MW, which is the sum of lower hybrid wave (LHW) heating power 2.8 MW and electron cyclotron resonance heating (ECRH) power 1.5 MW. Assuming that 20% of the total heating power is radiated from the core region, the power crossing the separatrix to the SOL, P_{sep}, is 3.44 MW, which accounts for approximately 80% of the total heating power. The toroidal magnetic field (B_t) points to the active X-point, i.e. favorable B_t direction with ion ∇B drift towards the upper divertor. After a certain amount of Ar seeding, the partial divertor plasma detachment over several power widths is achieved on the divertor target. The electron temperature near the strike point on the divertor target, $T_{e,tar}$ is 4 eV, and the perpendicular heat flux density, $q_{\perp,tar}$ is 0.5 MW·m^{-2}. The power reaching the target plates can be calculated from the formula $P_{tar} = 4q_{\perp,tar}\pi R_{tar}\lambda_{int}$. The difference between the P_{sep} and the total deposition power on the target plates is expected to be radiated mainly by the impurity Ar. Since there is a lack of diagnostic system for impurity concentration in EAST, the corresponding concentration is simply estimated based on the energy balance:[38] $P_{sep} = P_{total} - P_{rad,core} \approx 80\%P_{total}$ and $P_{tar} = P_{sep} - P_{rad}$. Here, P_{rad} represents the total radiated power from the boundary region, while P_{tar} denotes the power reaching the target plates. It is assumed that the impurity radiation is mainly responsible for the radiation power loss. The ionization process and charge exchange process also lead to radiation power loss during detachment, but their influence is signifi-

cant only within a small region near the target plate as shown in Fig. 4(a). So the corresponding impurity concentration can be estimated from the formula $n_e^2 c_Z L_Z \times 4\pi R_{tar}\lambda_{int} L_{div} = P_{rad}$. Here, the density n_e is taken as a typical value of 10^{20} m^{-3} in the divertor area and L_Z is the average radiative cooling rate, which is 1.5×10^{-31} W·m^3 and 3×10^{-32} W·m^3 for impurities Ar and Ne, respectively. Based on the above setting, the concentration of impurity Ar is estimated at 0.2%. The input settings for 1D modeling are as follows: $T_{e,tar} = 4$ eV, $q_{\perp,tar} = 0.5$ MW·m^{-2}, $c_Z = 0.2\%$ (Ar), $\lambda_q = 6$ mm, and $\lambda_{int} = 12$ mm, which are typical values on EAST.[39] The connection length $L_{||} = \pi R q_{95}$ from the target to the OMP is approximately 25 m. Here the safety factor q_{95} is 4.5 for shot #57417 and the large radius $R = 1.85$. The connection length in divertor region, L_{div} is estimated at 5 m, which is closely related to the length of divertor leg, i.e., the distance from X-point to the strike point on the target plate. It should be noted that we assume that the deposited heat flux at the target in the 1D modeling is mainly due to the plasma contribution, ignoring the contributions of radiative heat and neutrals energy loading.

Figure 4 shows the 1D model results corresponding to the experimental parameters of shot #57417. The radiation loss caused by charge exchange process and ionization process related to main ions is mainly concentrated near the divertor target, and the radiation loss of impurity Ar is the dominant in the whole region except for the area very close to the target as shown in Fig. 4. Along the flux tube from the OMP to the target plates, the temperature gradually decreases. The momentum loss occurs mainly in the vicinity of the target plate when the target electron temperature drops below 10 eV (see Fig. 4(a)). Due to the momentum conservation, the density of the plasma gradually increases away from the OMP. Near the divertor target plates, the density of the plasma drops significantly, which is caused by recombination and the friction exerted on the plasma by the collisions between ions and neutral atoms when the target plate temperature is low enough as shown in Fig. 4(a). The dotted line in Fig. 4(b) represents the change in power width at the entrance of the divertor L_{div}, which is broadened from λ_q to λ_{int}. According to the above input settings, the total power crossing the separatrix P_{sep} and the upstream electron temperature T_e calculated by the 1D model are 3.55 MW and 72.9 eV as listed in Table 2.

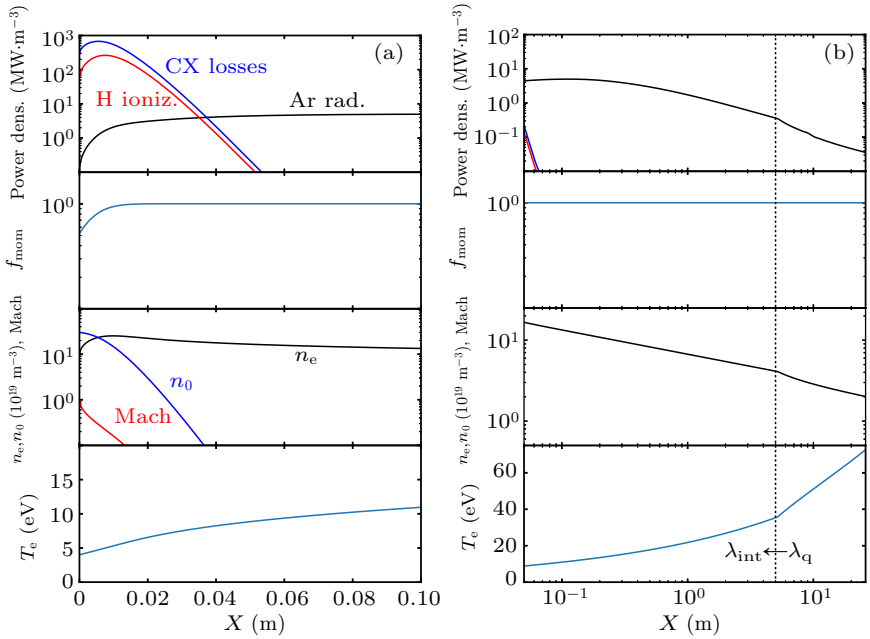


Fig. 4. Evolutions of plasma parameters, momentum loss factor, and radiative losses power density (Power dens.) close to target (a) and along flux tube to the OMP (b) calculated by 1D model. The 1D model parameter settings are as follows: $T_{e,tar} = 4$ eV, $q_{\perp,tar} = 0.5$ MW·m^{-2}, $c_Z = 0.2\%$ (Ar), $L_{div} = 5$ m, and $L_{||} = 25$ m. Dotted line represents the change in power width at the entrance of the divertor L_{div}, which is broadened from λ_q to λ_{int}.

The EAST shot #85293 is a typical upper single null configuration H-mode discharge with Ne impurity seeding.[7] The plasma has good core confinement $H_{98,y2} \sim 1.1$, and the basic parameters are as follows: I_p is 400 kA, B_t is 2.4 T, $\bar{n}_e$ is about 5.3×10^{19} m^{-3}, and P_{in} is 2.5 MW that is the sum of LHW (1.9 MW) and ICRH (0.6 MW). Assuming that 80% of the power crosses the separatrix, then $P_{sep} = 2.0$ MW. After a certain amount of Ne seeding, the partial divertor detachment occurrs. Compared with the attached condition without Ne seeding, the detached condition with Ne seeding can reduce the peak heat flux by about 80%. The $T_{e,tar}$ and $q_{\perp,tar}$ at the target drop to about 5 eV and 0.3 MW·m^{-2}, respectively. Similarly, the concentration of impurity Ne is estimated at 0.6%. The input settings for 1D modeling of Ne seeding case are as fol-

lows: $T_{e,tar} = 5$ eV, $q_{\perp,tar} = 0.3$ MW$\cdot$m^{-2}, $c_Z = 0.6\%$ (Ne), $\lambda_q = 6$ mm, $\lambda_{int} = 12$ mm, $L_{div} = 5$ m, and $L_{||} = 25$ m. As listed in Table 2, the P_{sep} and the upstream T_e calculated by the 1D model are 2.13 MW and 59.5 eV.

From Table 2, one can see that the divertor detachment with Ne or Ar impurity seeding in EAST can be well reproduced by the 1D model. The 1D model calculation results indicate that partial detachment of the divertor plasma can be achieved by seeding with either Ne or Ar, which is in consistency with the experimental observation in EAST.[7,37] It shows that seeding with a lower concentration of Ar impurity can achieve the partial divertor plasma detachment due to its stronger cooling capability. However, the experimental results in EAST indicate that seeding Ar always causes confinement to degrade in the divertor detachment state, while Ne seeding does not degrade the confinement performance and may even improve it,[40] which may be due to the relatively strong radiation loss in the core plasma with Ar impurity seeding.

Table 2. Comparison between 1D model and EAST experiments.

		Input		Output		
		$T_{e,tar}$ (eV)	$q_{\perp,tar}$ (MW$\cdot$m^{-2})	P_{sep} (MW)	P_{rad} (MW)	T_e (eV)
EAST#57417	Experiment	4	0.5	3.44	3.27	~ 70
	1D simulation	4	0.5	3.55	3.38	72.9
EAST#85293	Experiment	5	0.3	2.00	1.90	~ 55
	1D simulation	5	0.3	2.13	2.03	59.5

3.2. Comparison of 1D model and 2D simulation

To estimate the validity of the 1D model for the large size device with extremely high plasma parameters, the comparison between the 1D model simulation and the 2D simulation is also carried out for the China Fusion Engineering Test Reactor (CFETR). The CFETR is the next-step fusion device for the Chinese magnetic confinement fusion program with the major radius $I_p = 7.2$ m and the minor radius $a = 2.2$ m, the maximum operation plasma current $I_p = 14$ MA and the toroidal magnetic field $B_T = 6.5$ T.[2] According to the physics design of CFETR, it will produce a fusion power up to 1 GW in phase I, which corresponds to about 200 MW transported from the core region into the SOL to be exhausted.[41]

The operational points for CFETR detachment with Ne and Ar seeding simulated by the 1D model and 2D SOLPS-ITER code are compared in Table 3. The relevant physical parameters on the target for CFETR calculated by 2D SOLPS-ITER code under the detachment scenario are employed as the inputs for the 1D model.

For the case of Ne seeding, the parameter settings for the 1D modeling based on the 2D SOLPS-ITER simulation[41] are as follows: $T_{e,tar} = 2.8$ eV, $q_{\perp,tar} = 2.0$ MW$\cdot$m^{-2}, $c_Z = 0.8\%$ (Ne), $\lambda_q = 4$ mm, $\lambda_{int} = 14$ mm, $L_{div} = 15$ m, and $L_{||} = 125$ m, corresponding to the connection length from the target to the OMP. Based on the settings, the P_{sep} and the upstream T_e calculated by the 1D model are 202.9 MW and 258 eV respectively, which are in good agreement with the values of 200 MW and 290 eV used in 2D SOLPS-ITER code as listed in Table 3. The upstream T_e calculated by the 1D model is slightly lower than the 2D simulation result, which may be caused by underestimating the contribution of charge exchange process and ionization process in the power loss when the target electron temperature is very low.

For the case of Ar seeding, the $T_{e,tar}$ is 3.3 eV, the $q_{\perp,tar}$ is 2.5 MW$\cdot$m^{-2}, and the Ar impurity concentration is 0.2%. The P_{sep} and the upstream T_e calculated by the 1D model are 202.7 MW and 242 eV, respectively. They are also reasonably consistent with the values of the 2D modeling,[41] as listed in Table 3. The radiation efficiency with Ar seeding is higher than that with Ne seeding for CFETR. Under the same upstream power, the required concentration of Ar impurity is much lower than that of Ne impurity to achieve the divertor detachment. It may reduce the fuel dilution in core plasma to enhance the tritium burnup. However, due to the relatively strong radiation in the core for the Ar impurity, it may cause the core plasma performance to degrade. Therefore, it is very important to select the appropriate impurity to achieve divertor detachment and maintain high confinement performance of the core plasma.[42]

Table 3. Comparison of 1D model and SOLPS-ITER simulation of CFETR.

		Input		Output	
		$T_{e,tar}$ (eV)	$q_{\perp,tar}$ (MW$\cdot$m^{-2})	P_{sep} (MW)	T_e (eV)
CFETR 0.8% Ne seeding	SOLPS	2.8	2.0	200	~ 290
	1D simulation	2.8	2.0	202.9	258
CFETR 0.2% Ar seeding	SOLPS	3.3	2.5	200	~ 280
	1D simulation	3.3	2.5	202.7	242

4. Prediction and parameter scanning with 1D model

Although the physics in the 1D model may be greatly simplified, it has been proved to be reliable through comparison between the EAST experiments and the 2D SOLPS-ITER code. The predictions and parameter scanning of divertor detachment via impurity seeding for the EAST with high heating power scenarios and the CFETR with high fusion power scenarios in phase II by using the 1D model are presented in this section.

4.1. Prediction and parameter scanning for EAST

The required concentrations of impurities N_2, Ne, and Ar for the EAST with the $P_{sep} = 10$ MW and $I_p = 1$ MA discharges to achieve detachment are predicted in this subsection, in which the Greenwald density limit[29] n_{GW} is 1.27×10^{20} m^{-3}. Previous research shows that the divertor plasma can achieve the partial detachment with $T_{e,tar} \sim 10$ eV via impurity seeding.[43] The $T_{e,tar}$ and the $q_{\perp,tar}$ are respectively set to 10 eV and 6 MW$\cdot$m^{-2} on the divertor target in the 1D modeling. In this case, the upstream density calculated by the 1D model does not exceed $0.5n_{GW}$, which is the largest value ever achieved within the theoretical predictions for ballooning instability.[44] The prediction results show that seeding a certain concentration of N_2, Ne, and Ar can trigger off the occurrence of the divertor plasma detachment for EAST with high heating power scenarios, as listed in Table 4. For the EAST scenarios with the P_{sep} of about 10 MW, more than 80% of the total power P_{sep} crossing the separatrix must be radiated to achieve the divertor detachment. The 1D result indicates that seeding with a high concentration of N_2 impurity can achieve the partial divertor plasma detachment, it may cause the strong fuel dilution. Considering that Ar impurity may have relatively strong radiation from the core region, it is possible that the performance of core plasma to degrade. Therefore, compared with Ar seeding, Ne seeding may be many advantages in the compatibility between the plasma detachment and the high performance for EAST with high heating power scenarios, which is in agreement with experimental observations.[37,45]

Table 4. Prediction results with the 1D model for EAST.

$T_{e,tar}$ (eV)	$q_{\perp,tar}$ (MW·m^{-2})	Impurity	c_Z (%)	P_{sep} (MW)	P_{rad} (MW)	T_e (eV)	$n_{e,sep}/n_{GW}$
10	6	N_2	1.5	10.0	8.0	125.5	0.5
10	6	Ne	0.6	10.1	8.1	126.8	0.5
10	6	Ar	0.3	10.0	8.0	126.0	0.5

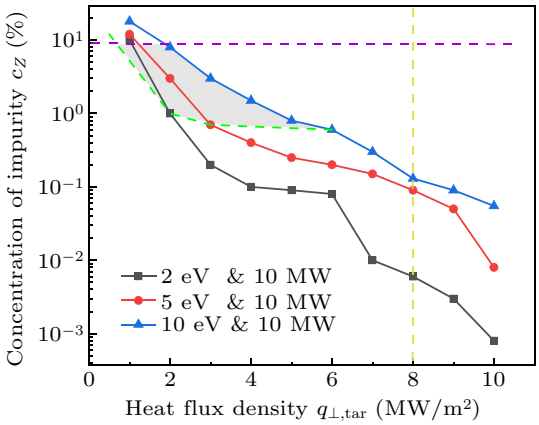


Fig. 5. Parameter scanning of EAST with Ne seeding, with grey area representing optimized parameter space for EAST divertor detachment.

The parameter space is scanned by the 1D model for EAST with the $P_{sep} = 10$ MW via Ne seeding as shown in Fig. 5. It is assumed that the maximum heat flux density that the target plate can withstand does not exceed the engineering limit of 10 MW$\cdot$m^{-2}, and only 8 MW$\cdot$m^{-2} is contributed by plasma. The case on the right side of the yellow dash line means that the total heat flux deposited on the target plate may exceed the engineering heat load limit of 10 MW$\cdot$m^{-2} on plasma facing components (PFCs). The purple dash line indicates the maximum divertor impurity Ne concentration $c_Z = 9\%$, corresponding to half the values allowed from the burn conditions under the assumption of the divertor enrichment value $E = 10$.[46] The green dash line corresponds to the upstream density value of $0.5n_{GW}$. Taking into account the constraints of target temperature (< 10 eV), density and heat flux limit, the grey area enclosed by the above lines in Fig. 5 represents relatively the optimized parameters space for EAST discharges with the $P_{sep} = 10$ MW. In this area, the divertor detachment and high performance for core plasma are well compatible.

4.2. Prediction and parameter scanning for CFETR

For phase II of CFETR, the fusion power (P_{fus}) will be more than 2 GW to demonstrate electric power generation.[2] So the selection of impurity species and the estimation of the required amount of impurity injection are also crucial for CFETR phase II with high fusion power scenarios. Previous study has shown that when the $T_{e,tar}$ is lower than 5 eV, the sputtering of the divertor target plate tungsten material is effectively suppressed, which can significantly extend the lifetime of the tungsten divertor components.[47] So the $T_{e,tar}$ is set to 5 eV. To keep the heat flux to PFCs below 10 MW$\cdot$m^{-2} level, the $q_{\perp,tar}$ contributed by plasma is set to 5 MW$\cdot$m^{-2}, on the assumption that the contribution of radiative heat to the

target heat flux reaches up to 5 MW · m^{-2}. For the CFETR, this is reasonable due to the high radiative power loss fraction to achieve divertor detachment.[10] The upstream temperature and the radiative power loss calculated from the 1D model are listed in Table 5. For CFETR phase II, more than 95% of the P_{sep} must be radiated to achieve the divertor detachment, which is approximately 395 MW. This result is comparable to the simulation of the JA-DEMO with fusion power of 2 GW via impurity seeding, where the ratio of the radiated power to the total exhausted power is about 92%.[48] Seeding Ne requires a relatively high concentration, which may lead to the severe fuel dilution, reducing the fusion power. It suggests that injection of higher Z impurities such as Ar and Kr with high radiative loss rate is beneficial to reducing the impurity concentration and diluting the fuel in the core plasma, thus enhancing the tritium burnup. This is in agreement with the reported simulations.[21,49] For phase II of CFETR, P_{heat} is much larger than the threshold power $P_{L\to H}$, so the core radiation from high Z impurity may be not a severe problem as mentioned in EU-DEMO and JA-DEMO.[50]

Table 5. Prediction results from 1D model for CFETR.

$T_{e,tar}$ (eV)	$q_{\perp,tar}$ (MW·m^{-2})	Impurity	c_Z (%)	P_{sep} (MW)	P_{rad} (MW)	T_e (eV)	$n_{e,sep}/n_{GW}$
5	5	Ne	1.0	401.9	394.4	308.0	0.5
5	5	Ar	0.55	400.0	392.5	312.0	0.5
5	5	Kr	0.4	401.2	393.7	327.1	0.5

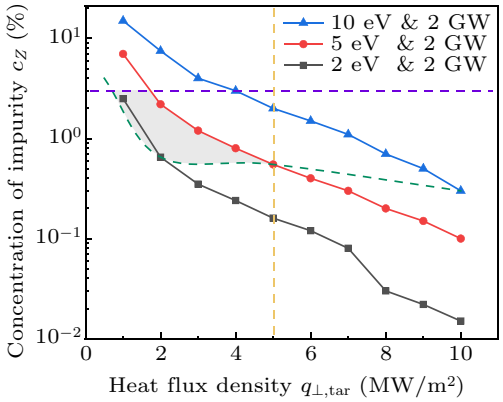


Fig. 6. Parameter scanning of CFETR phase II with Ar seeding, with grey area representing the optimized parameter space for CFETR divertor detachment.

The optimized parameters' space for CFETR phase II divertor detachment via Ar seeding is also determined by the 1D model as shown in Fig. 6. In order to maintain the total heat flux deposited on the target plate below the limit of 10 MW · m^{-2}, assuming that the contribution of radiative heat to the target heat flux is about 5 MW·m^{-2}, the case on the right side of the yellow dash line may exceed the limit. The maximum divertor impurity Ar concentration $c_Z = 3\%$ to satisfy the burning condition,[46] is shown by the purple dash line. The green dash line corresponds to the value $n_{e,sep}/n_{GW} = 0.5$.[44] Considering the constraints of target temperature (< 5 eV) required to effectively suppress the sputtering of tungsten components, impurity concentration, density and heat flux limits, the grey area enclosed by the above lines in the Fig. 6 represents a relatively optimal operation parameters space for CFETR phase II. The divertor detachment and high fusion power are well compatible in this area. Since impurity Kr has the relatively strong radiation capability than impurity Ar, the maximum divertor impurity Kr concentration will be lower. Therefore, the corresponding optimal operation parameters range with Kr seeding for CFETR phase II will be shifted downward.

5. Conclusions

In this study, a 1D modeling code for the impurity seeded detached divertor operational point is developed based on the Python language. It can perform quick parameter scanning, and thus predicting radiation and impurity concentrations of several impurity species and discharge conditions. An experiment for the onset of detachment by Ne and Ar seeding in EAST is well reproduced by using the 1D model. The comparison between the 1D modeling and 2D simulation by SOLPS-ITER code for CFETR detachment with Ne and Ar seeding also shows good consistency. The reliability of the 1D calculation is verified by comparing the 1D model with EAST experiments and 2D simulation results for CFETR. The radiative power loss and the requirement of the corresponding impurity concentration for achieving divertor detachment operation via N_2, Ne, and Ar seeding for the EAST with high heating power scenarios are predicted. It suggests that active injection of Ne in high heating power scenarios for EAST may be beneficial to both divertor detachment and core plasma performance. The optimized parameters space is scanned by the 1D model for EAST with the $P_{sep} = 10$ MW to achieve divertor detachment with Ne seeding. Additionally, the radiative power loss and the corresponding impurity concentration required to achieve divertor detachment operation by Ne, Ar, and Kr seeding for phase II of the CFETR are predicted. The results indicate that active injection of higher Z impurity with high radiative loss rate is beneficial to decreasing the impurity concentration, thereby reducing the fuel dilution. Furthermore, the optimal parameters space for CFETR phase II divertor detachment via Ar seeding is also determined by the 1D model. The 1D modeling code that is developed and used in this work has some caveats which should be mentioned. It calculates a steady-state result, and in experimental conditions the divertor radia-

tion experiences time-varying effects particularly in the region near the X-point, which are caused by the physical processes such as edge localized modes (ELMs).[51] Although appropriate non-coronal parameters can capture these time-varying effects to some extent, time-varying modeling and detachment control will be the focus in the future research. In addition, the development of diagnostic techniques for directly measuring impurity concentration in the divertor region will greatly enhance quantitative research on divertor detachment.

Acknowledgements

The authors would like to thank Hang Si for providing the CFETR simulation data and EAST Team for the support in EAST experiment.

Project supported by the National Key Research and Development Program of China (Grant No. 2022YFE03030001) and the National Natural Science Foundation of China (Grant No. 12075283).

References

[1] Gunn J P, Carpentier-Chouchana S, Escourbiac F, Hirai T, Panayotis S, Pitts R A, Corre Y, Dejarnac R, Firdaouss M, Kočan M, Komm M, Kukushkin A, Languille P, Missirlian M, Zhao W and Zhong G 2017 *Nucl. Fusion* **57** 046025
[2] Zhuang G, Li G Q, Li J, Wan Y X, Liu Y, Wang X L, Song Y T, Chan V, Yang Q W, Wan B N, Duan X R, Fu P and Xiao B J 2019 *Nucl. Fusion* **59** 112010
[3] Kallenbach A, Bernert M, Beurskens M, Casali L, Dunne M, Eich T, Giannone L, Herrmann A, Maraschek M, Potzel S, Reimold F, Rohde V, Schweinzer J, Viezzer E and Wischmeier M 2015 *Nucl. Fusion* **55** 053026
[4] Covele B, Kotschenreuther M, Mahajan S, Valanju P, Leonard A, Watkins J, Makowski M, Fenstermacher M and Si H 2017 *Nucl. Fusion* **57** 086017
[5] Jaervinen A E, Giroud C, Groth M, *et al*. 2016 *Nucl. Fusion* **56** 046012
[6] Nakano T and Asakura N 2019 *Nucl. Mater. Energy* **18** 356
[7] Meng L Y, Wang L, Wang H Q, *et al*. 2022 *Nucl. Fusion* **62** 086027
[8] Reinke M L, Hughes J W, Loarte A, Brunner D, Hutchinson I H, LaBombard B, Payne J and Terry J L 2011 *J. Nucl. Mater.* **415** S340
[9] Wischmeier M 2015 *J. Nucl. Mater.* **463** 22
[10] Liu X J, Xu G L, Ding R, Jia G Z, Sang C F, Si H, Nian F F, Yang Z S, Li G Q, Chan V S, Deng G Z, Gao S L and Gao X 2020 *Phys. Plasmas* **27** 092508
[11] Canik J M, Briesemeister A R, Lasnier C J, Leonard A W, Lore J D, McLean A G and Watkins J G 2015 *J. Nucl. Mater.* **463** 569
[12] Dudson B D, Allen J, Body T, Chapman B, Lau C, Townley L, Moulton D, Harrison J and Lipschultz B 2019 *Plasma Phys. Control. Fusion* **61** 065008
[13] Togo S, Nakamura M, Ogawa Y, Shimizu K, Takizuka T and Hoshino K 2013 *Plasma Fusion Res.* **8** 2403096
[14] Derks G L, Frankemölle J P K W, Koenders J T W, van Berkel M, Reimerdes H, Wensing M and Westerhof E 2022 *Plasma Phys. Control. Fusion* **64** 125013
[15] Zhou Y, Dudson B, Militello F, Verhaegh K and Myatra O 2022 *Plasma Phys. Control. Fusion* **64** 065006
[16] Nakamura M, Togo S, Ito M and Ogawa Y 2011 *Plasma Fusion Res.* **6** 2403098
[17] Tsubotani Y, Tatsumi R, Hoshino K and Hatayama A 2019 *Plasma Fusion Res.* **14** 2403108
[18] Siccinio M, Fable E, Lackner K, Scarabosio A, Wenninger R P and Zohm H 2016 *Plasma Phys. Control. Fusion* **58** 125011
[19] Reinke M 2017 *Nucl. Fusion* **57** 034004
[20] Zohm H 2019 *J. Fusion Energy* **38** 3
[21] Wenninger R, Arbeiter F, Aubert J, *et al*. 2015 *Nucl. Fusion* **55** 063003
[22] Eich T, Sieglin B, Scarabosio A, Fundamenski W, Goldston R J, Herrmann A and Team A U 2011 *Phys. Rev. Lett.* **107** 215001
[23] Stangeby P C and Leonard A W 2011 *Nucl. Fusion* **51** 063001
[24] Post D, Abdallah J, Clark R E H and Putvinskaya N 1995 *Phys. Plasmas* **2** 2328
[25] Kallenbach A, Bernert M, Dux R, Reimold F and Wischmeier M 2016 *Plasma Phys. Control. Fusion* **58** 045013
[26] Eich T, Leonard A W, Pitts R A, Fundamenski W, Goldston R J, Gray T K, Herrmann A, Kirk A, Kallenbach A, Kardaun O, Kukushkin A S, LaBombard B, Maingi R, Makowski M A, Scarabosio A, Sieglin B, Terry J and Thornton A 2013 *Nucl. Fusion* **53** 093031
[27] Xu X Q, Li N M, Li Z Y, Chen B, Xia T Y, Tang T F, Zhu B and Chan V S 2019 *Nucl. Fusion* **59** 126039
[28] ADAS manual and documentation 2016 www.adas.ac.uk/manual.php
[29] Goldston R J, Reinke M L and Schwartz J A 2017 *Plasma Phys. Control. Fusion* **59** 055015
[30] Kallenbach A, Bernert M, Dux R, Casali L, Eich T, Giannone L, Herrmann A, McDermott R, Mlynek A, Müller H W, Reimold F, Schweinzer J, Sertoli M, Tardini G, Treutterer W, Viezzer E, Wenninger R and Wischmeier M 2013 *Plasma Phys. Control. Fusion* **55** 124041
[31] Stangeby P C 2018 *Plasma Phys. Control. Fusion* **60** 044022
[32] Huang J, Suzuki Y, Nojiri K and Ashikawa N 2021 *Plasma Sci. Technol.* **23** 084001
[33] Du H L, Sang C L, Wang L, Bonnin X, Wang H Q, Sun J Z and Wang D Z 2017 *Nucl. Fusion* **57** 116022
[34] Chen L, Xu G S, Yan N, *et al*. 2018 *Phys. Plasmas* **25** 072504
[35] Lin X, Yang Q Q, Xu G S, *et al*. 2021 *Nucl. Fusion* **61** 026014
[36] Xu J C, Wang L, Xu G S, Luo G N, Yao D M, Li Q, Cao L, Chen L, Zhang W, Liu S C, Wang H Q, Jia M N, Feng W, Deng G Z, Hu L Q, Wan B N, Li J, Sun Y W and Guo H Y 2016 *Rev. Sci. Instrum.* **87** 083504
[37] Chen J B, Duan Y M, Yang Z S, Wang L, Wu K, Li K D, Ding F, Mao H M, Xu J C, Gao W, Zhang L, Wu J H and Luo G N 2017 *Chin. Phys. B* **26** 095205
[38] Chen Y P, Wang F Q, Zha X J, Hu L Q, Guo H Y, Wu Z W, Zhang X D, Wan B N and Li J G 2013 *Phys. Plasmas* **20** 022311
[39] Deng G Z, Xu J C, Liu X, *et al*. 2018 *Plasma Phys. Control. Fusion* **60** 045001
[40] Li K D, Yang Z S, Wang H Q, *et al*. 2021 *Nucl. Fusion* **61** 066013
[41] Si H, Ding R, Senichenkov I, Rozhansky V, Molchanov P, Liu X J, Jia G Z, Sang C F, Mao S F, Chan V and the CFETR Team 2022 *Nucl. Fusion* **62** 026031
[42] Liu X J, Deng G Z, Wang L, Liu S C, Zhang L, Li G Q and Gao X 2017 *Phys. Plasmas* **24** 122509
[43] Wang L, Wang H Q, Eldon D, *et al*. 2022 *Nucl. Fusion* **62** 076002
[44] Eich T, Goldston R J, Kallenbach A, Sieglin B and Sun H J 2018 *Nucl. Fusion* **58** 034001
[45] Chu Y Q, Zhang B S, Li P, Yang X D, Liu H Q, Jie Y X, Wu C B, Zhang W M, Li K D, Zhou T F, He L, Zang Q, Lian H, Zhong F B, Zhu R J, Zhang L F and Hanada K 2023 *Nucl. Fusion* **63** 086021
[46] Kallenbach A, Bernert M, Dux R, Eich T, Henderson S S, Pütterich T, Reimold F, Rohde V and Sun H J 2019 *Nucl. Mater. Energy* **18** 166
[47] Kallenbach A, Balden M, Dux R, Eich T, Giroud C, Huber A, Maddison G P, Mayer M, McCormick K, Neu R, Petrie T W, Pütterich T, Rapp J, Reinke M L, Schmid K, Schweinzer J and Wolfe S 2011 *J. Nucl. Mater.* **415** S19
[48] Hoshino K, Asakura N, Shimizu K, Tokunaga S, Takizuka T, Someya Y, Nakamura M, Utoh H, Sakamoto Y and Tobita K 2014 *Plasma Fusion Res.* **9** 3403070
[49] Asakura N, Hoshino K, Homma Y and Sakamoto Y 2021 *Nucl. Mater. Energy* **26** 100864
[50] Asakura N, Hoshino K, Kakudate S, Subba F, You J H, Wiesen S, Rognlien T D, Ding R and Kwon S 2023 *Nucl. Mater. Energy* **35** 101446
[51] Bernert M, Eich T, Burckhart A, Fuchs J C, Giannone L, Kallenbach A, McDermott R M, Sieglin B and Team A U 2014 *Rev. Sci. Instrum.* **85** 033503